ACS NANO

www.acsnano.org

ARTICLE

Impact of Isovalent and Aliovalent Doping on Mechanical Properties of Mixed Phase $BiFeO_3$

Yooun Heo,[†] Songbai Hu,[†] Pankaj Sharma,[†] Kwang-Eun Kim,[§] Byung-Kweon Jang,[§] Claudio Cazorla,[†,‡] Chan-Ho Yang,[§,∥] and Jan Seidel*[,†]

[†]School of Materials Science and Engineering and [‡]Integrated Materials Design Centre, University of New South Wales (UNSW) Australia, Sydney, New South Wales 2052, Australia

[§]Department of Physics and [∥]Institute for the NanoCentury, Korea Advanced Institute of Science and Technology (KAIST), Daejeon 305-701, Republic of Korea

ABSTRACT: **In this study, we report the effect of doping in morphotropic $BiFeO_3$ (BFO) thin films on mechanical properties, revealing variations in the elasticity across the competing phases and their boundaries. Spectroscopic force−distance (*F*−*D*) curves and force mapping images by AFM are used to characterize the structure and elastic properties of three BFO thin-film candidates (pure-BFO, Ca-doped BFO, La-doped BFO). We show that softening behavior is observed in isovalent La-doped BFO, whereas hardening is seen in aliovalent Ca-doped BFO. Furthermore, quantitative *F*−*D* measurements are extended to show threshold strengths for phase transitions, revealing their dependence on doping in the system. First-principles simulation methods are also employed to understand the observed mechanical properties in pure and doped BFO thin films and to provide microscopic insight on them. These results provide key insight into doping as an effective control parameter to tune nanomechanical properties and suggest an alternative framework to control coupled ferroic functionalities at the nanoscale.**

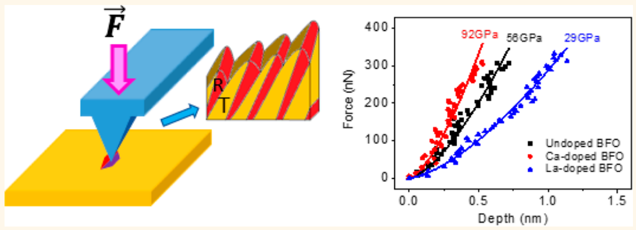

KEYWORDS: *nanostructure, morphotropic phase boundary, ferroelectrics, multiferroics, atomic force microscopy, elastic modulus, density functional theory*

The morphotropic phase boundary (MPB),[1,2] highly desired in lead based piezoelectrics, is a finite phase transition region between competing ferroelectric phases with energy proximity in the phase diagram.[3,4] The coexistence of low symmetry phases is observed at the MPB, bridging phases with different crystal symmetries.[5] Piezoelectrics based on such a transition region are found to display large electromechanical responses due to structural transitions and polarization rotation under an external stimulus such as electric field or stress, leading to a variety of applications such as sensors and actuators. The MPB in the lead-based systems can be driven by both chemical doping and strain, but chemically simple and lead-free alternative materials have been sought after for suitable applications. In this context, $BiFeO_3$ (BFO) has drawn considerable attention as a prototype multiferroic due to several intriguing functional properties such as magnetoelectric and electromechanical coupling,[6] photovoltaic effect,[7] domain wall conductivity,[8] and bias-induced metal−insulator transitions.[9] Moreover, the recent discovery of a strain-driven MPB in BFO films grown on (001) $LaAlO_3$ (LAO) substrates has led to numerous studies.[10−18]

Triggered by advances in thin-film engineering, epitaxial strain is used to tune the ground state of BFO thin films from the bulk like rhombohedral phase to the MPB region, consisting of low-symmetry rhombohedral-like (R) and tetragonal-like (T) phases.[10] Furthermore, doping by composition tuning with specific chemical elements is an effective route to induce structural transitions for enhanced functional properties of BFO.[19] Promising concepts of nanoscale domain and domain wall engineering through strain and chemical doping have been demonstrated, enabling the fabrication of almost pure T-phase in BFO.[20−22] Indeed, this T-phase has an extremely large c/a ratio of around 1.25 due to high in-plane compressive strain as a result of the lattice mismatch of around 4.5% between BFO and the underlying LAO substrate. Epitaxial stabilization of the T-phase is of great interest due to its high polarization value of over 150 $\mu C\ cm^{-2}$, significantly larger than its R-phase counterpart.[23] Highly strained BFO films grown on LAO substrates exhibit mixed-phase regions consisting of T- and R-phases with their relative fraction dependent on the thickness of the film. In these films, R needle-shaped domains are embedded into a T-phase matrix, with capacity to selectively switch between the two phases by application of external

Received: November 22, 2016
Accepted: February 22, 2017
Published: February 22, 2017

DOI: 10.1021/acsnano.6b07869
ACS Nano 2017, 11, 2805−2813

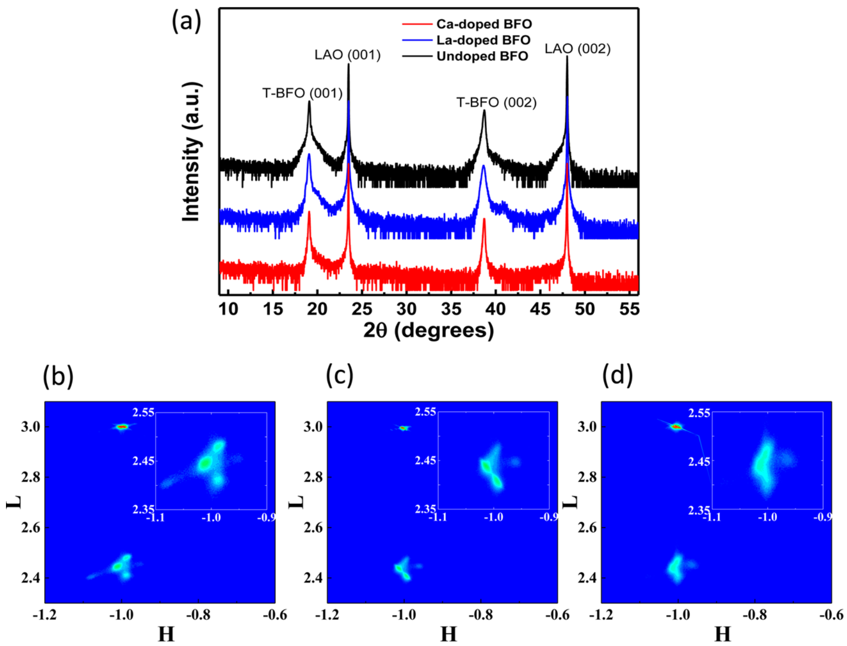

Figure 1. Structural characterization of the thin bismuth ferrite films by XRD (a) θ-2θ profiles around the (002) LAO diffraction peak for all of the BFO samples and (b) RSMs for (−103) diffraction peaks for (b) undoped BFO, (c) Ca-doped BFO, and (d) La-doped BFO, respectively.

electric field.[20] Moreover, a variety of other SPM-based control techniques were implemented for T−R phase transitions and the creation of nanoscale mixed phase regions with specific spatial orientations.[24−27] It was also revealed that the T−R mixture shows a giant piezoelectric coefficient, enabled by phase boundary motion.[20] Lately, sizable magnetic moments were identified within the distorted R-phase rather than at the boundaries, and altered magnetic structure of BFO through strain engineering has been reported.[28,29] In addition, a strong correlation between local strain state and the electronic properties at isosymmetric phase boundaries in mixed phase Ca-doped BFO was found.[30] In mixed phase BFO however, the role of the phase boundary is poorly understood in terms of mechanical properties including its elastic susceptibility and behavior. Very recently, mechanical switching and strict control of phase boundaries has been demonstrated in morphotropic BFO, and consequently extraordinary soft elastic behavior was observed during the phase transformation.[31] The fundamental understanding of mechanical properties of such boundaries may present not only an intriguing aspect of oxide interface functionality but also a crucial clue for unveiling the already observed material properties and physical phenomena. Moreover, control of mechanical properties in this system can provide a route to enhance and alter coupled functional properties.[32]

Here, we have characterized mechanical properties of three BFO samples: undoped, Ca-doped, and La-doped BFO thin films by employing scanning probe-based spectroscopic force−distance (*F*−*D*) measurements and force−volume mapping for elastic properties using AFM. First-principles computational techniques based on density functional theory (DFT) have been employed to rationalize the atomistic mechanisms underlying our observations. We reveal the impact of doping on elastic properties and nanoscale phase transition threshold strength. Our results suggest doping as an effective way of tuning nanomechanical properties and strain environment to control coupled ferroic functionality from device perspectives.

As a prototype system, we have chosen three BFO samples with similar thicknesses, undoped (61 nm), 2% Ca-doped (80 nm), and 5% La-doped (60 nm) thin films grown on LAO substrate, consisting of mixed phase morphology in the as-grown state. Doping with Ca as an aliovalent variant leads to large changes in oxygen vacancies in the material as compared to the undoped case,[33] while isovalent La doping does not alter the oxygen content significantly.[9,22,33,34] Note that the doping percentage can be strictly controlled in $Bi_{1-x}A_xFeO_{3-x}$ (A = Ca, La)[9,35] and that both 2% Ca-doped and 5% La-doped samples show a monoclinic ferroelectric state. Phase transformation occurs when sufficient force (*i.e.*, 50−100 MPa) is applied by the tip. A schematic overview of this is shown in the abstract. In order to study the impact of doping on mechanical properties, we performed force−volume mapping imaging, which involves acquisition of the spectroscopic *F*−*D* curves over a grid of consisting of 200 × 200 points. *F*−*D* curves are acquired by sweeping the *c*-axis parameter of the scanner at each point on a grid, such that a variable loading force is exerted by the AFM tip. For accurate quantitative measurements, we precisely calibrated the AFM cantilever used in this study. For this we have adopted the relation of Hooke's law as the following:

$$F = k \times Z \qquad (1)$$

where k is the spring constant of the cantilever, and z is vertical displacement of the tip. For this calibration, two parameters are required: (1) the optical lever sensitivity s of the detection optical beam system, and (2) the spring constant k of the cantilever. Both of these parameters are obtained by routine AFM calibrations.[32] The loading force exerted by the tip causes elastic deformation on the sample surface, wherein these spectroscopic *F*−*D* curves are analyzed in order to generate images with contrast for elastic information. Slopes of the curves contain information about the elastic deformation regime which can be extracted to yield a quantitative measure of Young's modulus.

DOI: 10.1021/acsnano.6b07869
ACS Nano 2017, 11, 2805−2813

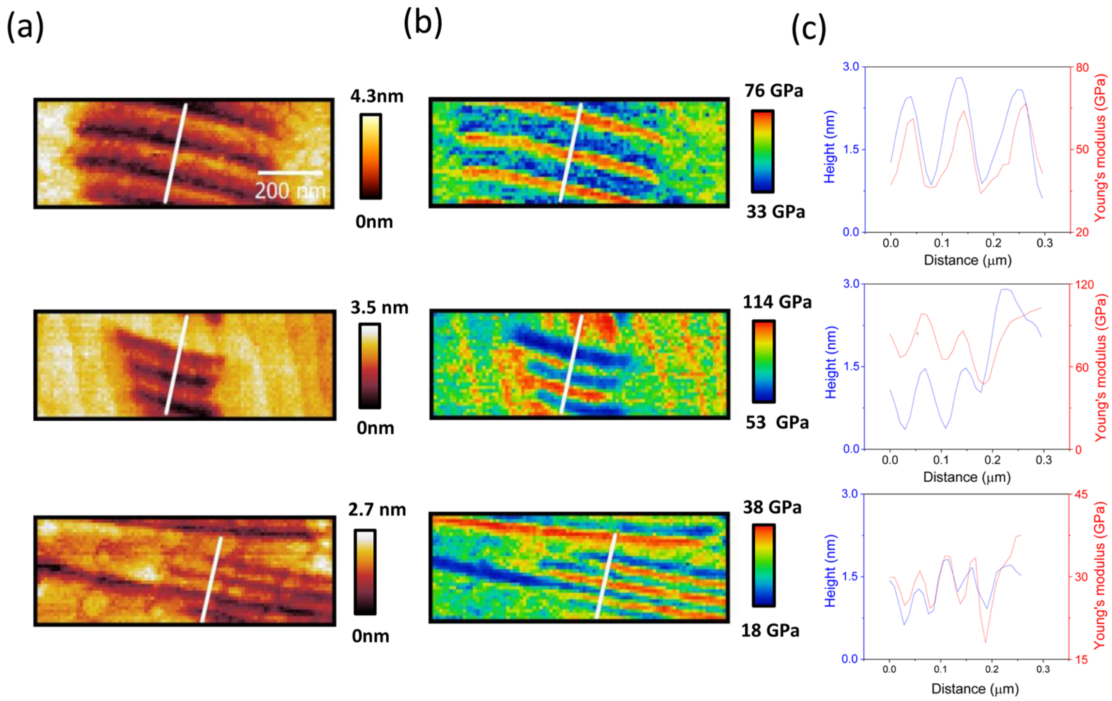

Figure 2. Comparison of (a) topography scan images and (b) 2D elastic stiffness mapping images of undoped, Ca-doped, and La-doped BFO (from up to down). (c) Cross-section profiles of surface features and stiffness for these films in the same order from up to down for undoped, Ca-doped, and La-doped BFO show elastic behavior across phase boundaries.

Within the framework of a Hertzian model, the relationship between loading force F_{load}, and elastic deformation depth d is given by the following:

$$F_{load} = \frac{4}{3}E^{*}R^{1/2}d^{3/2} \quad (2)$$

where E^* is the reduced modulus of the sample, and R is the radius of curvature of the tip (~50 nm). The reduced modulus is related to Young's modulus *via* the following equation:

$$\frac{1}{E^{*}} = \frac{1-\nu^{2}}{E} + \frac{1-{\nu_{tip}}^{2}}{E_{tip}} \quad (3)$$

where ν and E are the Poisson's ratio and effective Young's modulus of the sample ($\nu \sim 0.25$ for BFO), while ν_{tip} and E_{tip} are the Poisson's ratio and Young's modulus of the AFM-tip. It is assumed that E_{tip} (diamond tip) is much greater than the effective modulus of the film, and thus, the effective Young's modulus can be calculated using the Poisson's ratio of the BFO film. We assured that this model is valid for measuring the elasticity of standard reference samples as demonstrated in the Supporting Information of our previous report.[32] Therefore, using the Hertzian model, analysis of such spectroscopic F–D curves (force *versus* depth) provides the effective Young's modulus for the structural phase variants in the mixed phase regions. Based on these measurements, statistics of Young's modulus and threshold strength of phase transition are found for each BFO sample. Concerning the small difference of thickness and doping percentage between the samples used in this study, it should be noted that such comparison is validated for studying doping effects on mechanical properties, by the concept of analysis of variance (ANOVA), concluding that difference in thickness of 10–20 nm and doping percentage of 2–3% is rather negligible, as verified by similar values of elastic modulus between 35 nm and 50–60 nm-thick pure BFO films (thickness comparison) and 5% and 10% La-doped BFO films (percentage of doping comparison). Therefore, differences in elastic properties between samples likely result from types of doping in BFO.

RESULTS AND DISCUSSION

Figure 1a shows θ-2θ profiles around the (002) LAO Bragg reflections for undoped, Ca-doped, La-doped BFO films. All of these films only show the (002) BFO diffraction peaks without any reflections from impurity phases, confirming the high quality of the materials. Indeed, these peaks correspond to T-like phase of BFO, while all these samples contain mixed phase regions, wherein the R-like phase is not resolved in the θ-2θ scans due to its relatively small fraction within the films. Further investigations by reciprocal space maps (RSMs) for (−103) diffraction peaks conclude that the T-like phase of all the BFO thin films has M_C-type splits of the (−103) peaks, clearly showing monoclinic distortion of the T-like phase (Figure 1b–d). We note that also the peak as part of the unit cell structures of mixed phase is detected. There is no transverse shift between the BFO and LAO diffraction spots, indicating all these thin films are fully strained by the substrate.

AFM topography scan images show atomically flat surfaces in all three films with mixtures of bright T-like phase (T-phase) and dark R-like phase (R-phase) stripes due to their difference in *c*-axis parameter (Figure 2a). It is interesting to note the characteristic feature of long R-phase stripes in the La-doped BFO thin film due to anisotropic strain relaxation from La-doping.[36] Elastic properties are imaged within the same region of topography for all the BFO films (Figure 2b). Note that highly strained BFO thin films have shown mechanical softening where its elastic modulus is roughly an order of magnitude lower than BFO in the bulk form.[37−39] Force–volume mapping images show relative changes of Young's modulus of pure T-phase, R-phase and phase boundaries (R–T

DOI: 10.1021/acsnano.6b07869
ACS Nano 2017, 11, 2805–2813

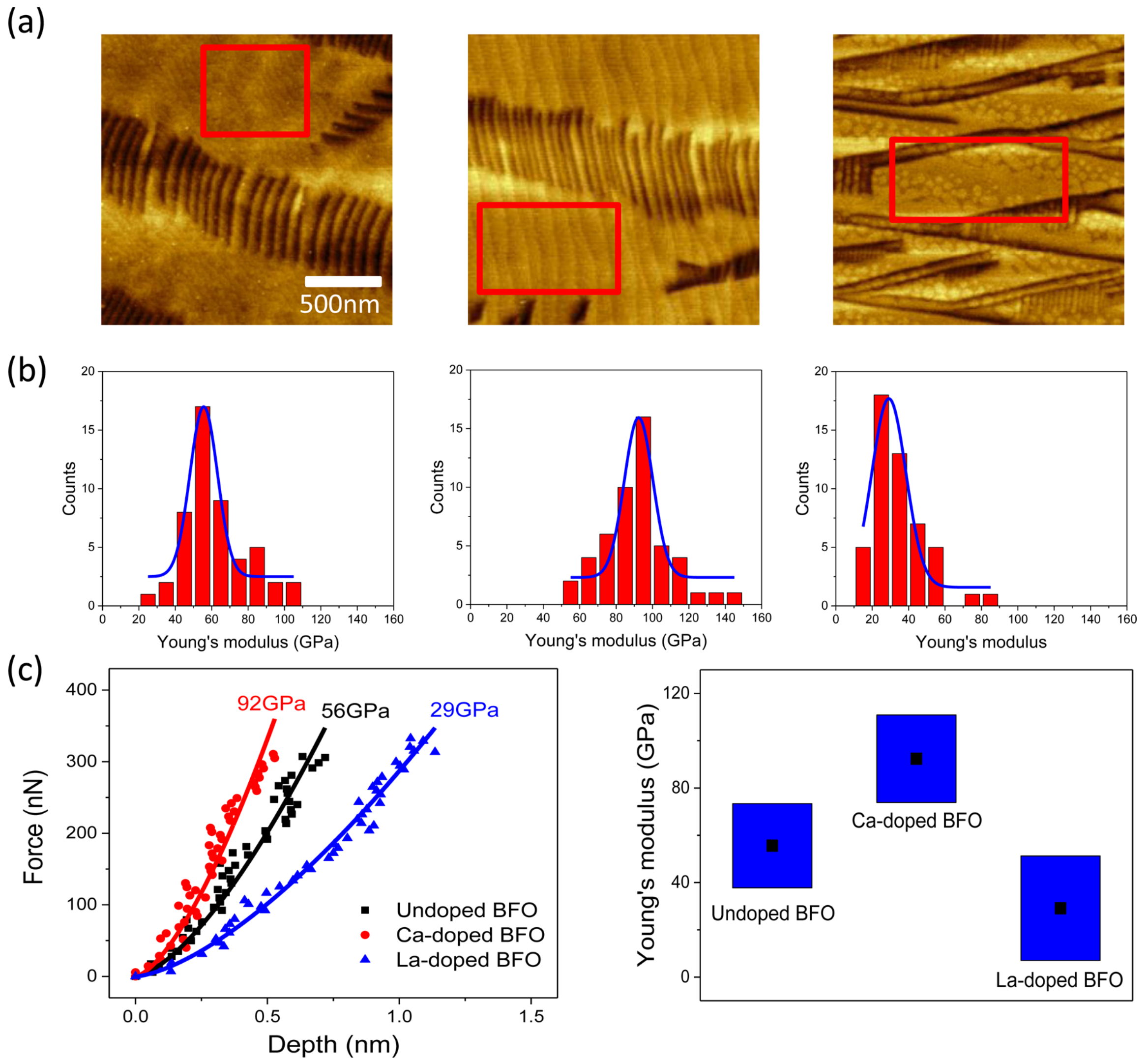

Figure 3. Statistical analysis of stiffness: (a) Topography images as a representative area with a red square box for *F*−*D* measurements to extract the Young's modulus and (b) statistics of the Young's modulus with Gaussian fit for undoped, Ca-doped, and La-doped BFO (from up to down order). (c) Stress−strain curves (left) with the slope in elastic regime and floating column plot (right) for the average Young's modulus with ranges of error for each BFO thin film.

and T−R). Based on these images, we find the overall trend that Young's modulus of the pure T-phase is higher than that of R-phase, indicating the T-phase is relatively stiff and the R-phase is soft in all of these films regardless of doping in BFO. This trend is in agreement with the observed electromechanical response and theoretical calculations based on a thermodynamic approach.[20,32,40,41] Moreover, local elastic properties of pure BFO thin films measured by ultrasonic force microscopy (UFM) follow the same trend.[42] We also note that similar elastic behavior is seen in all BFO films such that the T-phase near the phase boundary is stiffer than the pure-T-phase region. This is reflected in the sharp boundary contrast between T-phase and R-phase. Comparison of cross section profiles of topography and elastic mapping image shows a clear trend of elasticity across phase boundaries (Figure 2c). We find that a peak and trough of elastic modulus are mostly found in the vicinity of T- and R- phase, respectively, in all of these films. This trend was ensured after statistical comparison over wider mixed phase regions. On the other hand, numerical values of Young's modulus for pure T-phase show differences between the three BFO samples. These results therefore reveal variations of the strain environment of the films upon doping of the system.

In order to statistically analyze mechanical properties between these BFO samples, we carried out *F*−*D* curve measurements on pure T-phase regions for up to 50 cycles for each BFO sample. Topography scan images (Figure 3a) for pure-BFO, Ca-doped BFO, and La-doped BFO are shown with a red square box as a reference area, which are representative for all the *F*−*D* curves and numerical data of Young's modulus obtained. For these measurements, we selected locations of pure T-phase areas that are free of R-phases in close proximity. As a result, histogram plots of Young's modulus with Gaussian fit are presented in Figure 3b. The representative *F*−*D* curves in the elastic regime for each BFO sample are shown in Figure 3c. We find from a statistical analysis of up to 50 data points that the average Young's moduli of T-phase for undoped, Ca-doped and La-doped are roughly 56 ± 17, 92 ± 18, and 29 ± 22 GPa, respectively. Therefore, these results demonstrate that isovalent and aliovalent doping can change the mechanical stiffness of BFO thin films.

DOI: 10.1021/acsnano.6b07869
ACS Nano 2017, 11, 2805−2813

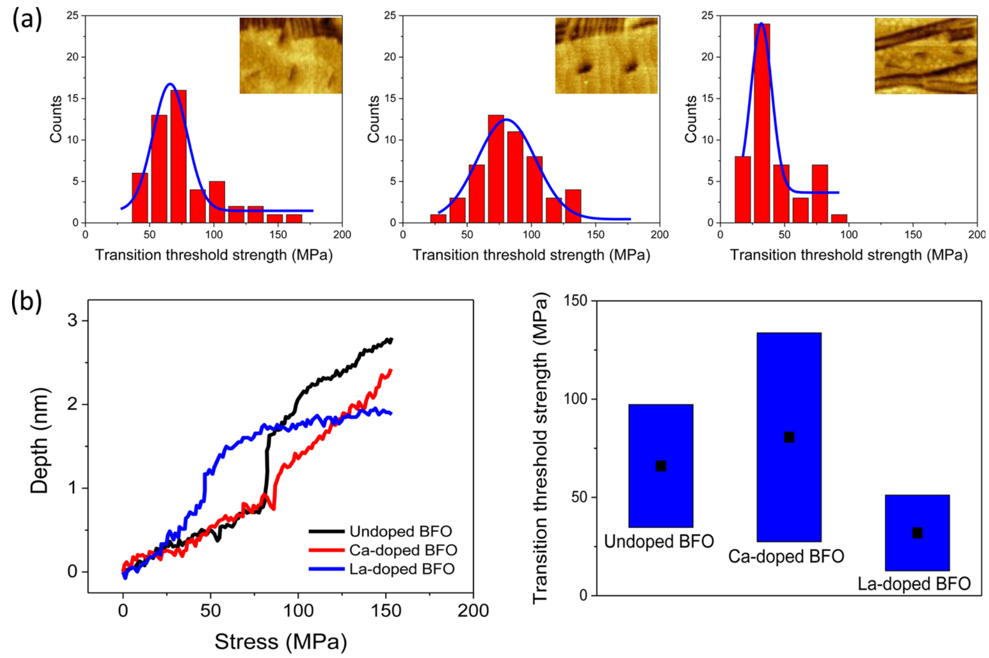

Figure 4. Phase transition behavior from locally applied force and transition threshold strength: (a) Statistics of transition threshold strength for undoped, Ca-doped, and La-doped BFO. Inset figures are topography scan images with formation of dark R-phase stripes after force-induced switching. (b) Depth *versus* stress curves (left) that show switching behavior from the distinguished kinks and floating column plot (right) for average transition threshold strength with ranges of error for each BFO thin film.

For a more complete understanding, we also perform force switching measurements on these BFO thin films by extending the force range beyond the elastic regime to find the phase transition threshold strengths. Consequently, at higher forces, the phase transformation occurs from T-phase to R-phase, creating a R-phase dot or stripe. This was previously reported in the strain-driven morphotropic BFO system.[31] Phase switching is observed by a prominent kink in the *F*−*D* curves, allowing us to find the transition force. We confirmed that phase switching occurs by checking the formation of stripe R-phase from a comparison of topography scan images taken before and after running local *F*−*D* curve measurements. Based on the contact area approximated by the radius of curvature of the tip, the phase transition force is converted to strength. Statistics of transition threshold strength are presented as histogram plots with Gaussian fitting to compare softening behavior during force-induced switching measurements (Figure 4a). Inset images show representative locations for all the measurements, where R-phase is created due to phase transformation. The representative depth *versus* stress curves for the BFO films are also shown to compare transition strength values (Figure 4b). Based on these results, we find the phase transition threshold strengths for pure BFO, Ca-doped, and La-doped BFO are roughly 700 ± 300, 800 ± 500, and 300 ± 200 MPa, respectively, following the same trend of the Young's modulus (Figure 3b). For phase transition, Ca-doped BFO requires greater threshold strength than pure-BFO, however the difference is small, proving similar strain environments for the T-phase in these samples. However, La-doped BFO only requires nearly half of that force for phase switching, indicating a very soft strain environment and vulnerability to mechanical force for structural phase transitions. These results imply that doping can impact the elasticity of BFO thin films at the atomic level, and further investigation is required. It is also worthwhile to consider the characteristic environment of La-doped BFO with its few micron-long stripes[36] due to a considerably lower strain state from La-doping. Therefore, this finding provides considerable insight into doping effects on local strain and elasticity of BFO, whose implications may be also correlated to intriguing phenomena reported earlier including giant electromechanical response[20] and anisotropic phase boundary conductivity.[30] Furthermore, control of doping and hence elastic properties in BFO can be further exploited to develop other correlated functionalities such as nonvolatile strain conductivity[43] and enhanced coupling between ferroelastic and ferroelectric order for nanoelectronics.[44−46]

For gathering microscopic insight, we performed first-principles simulations based on DFT methods. Our calculations predict a first-order phase transition between a R-like and a T-like phase in BFO thin films at epitaxial strains of $\eta \approx -3\%$ (see Figure 5a,b and ref 47). Both R and T crystals present monoclinic symmetry and can be assigned to the space group *Cc*.[47,48] As it is shown in Figures 5a,b, the R-phase is characterized by an electrical polarization that is tilted with respect to the out-of-plane direction, a c/a ratio close to unity, and significant antiphase oxygen octahedral rotations along the three Cartesian directions; its ground-state spin magnetic order can be described as *G*-type antiferromagnetism (*i.e.*, neighboring magnetic spins align antiparallel both in-plane and out-of-plane). The T-phase, on the other hand, presents a large electrical polarization mostly oriented along the out-of-plane direction, accompanied of a huge c/a ratio and practically negligible antiferrodistortive O_6 rotations;[47] its ground-state spin magnetic order can be described as *C*-type antiferromagnetism (*i.e.*, neighboring magnetic spins align antiparallel in-plane and parallel out-of-plane).[49]

In Figure 5c, we present our DFT Young's modulus results obtained in pure and doped T-like BFO thin films at $\eta = -4.5\%$ (*i.e.*, we considered an in-plane lattice parameter of 3.72 Å).

DOI: 10.1021/acsnano.6b07869
ACS Nano 2017, 11, 2805−2813

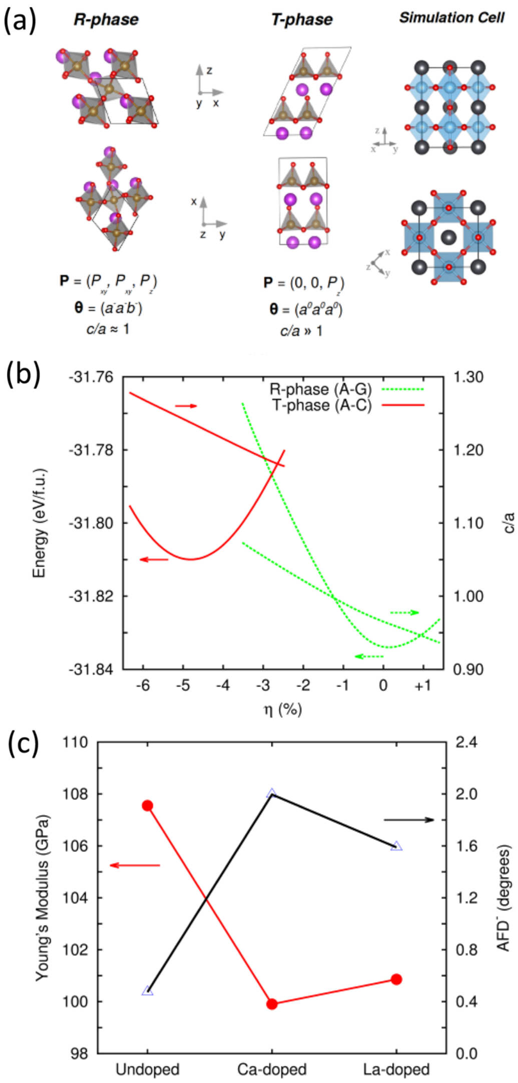

Figure 5. Details and results of our DFT calculations performed in stoichiometric BFO-based thin films. (a) Sketch of the R- and T-phases found in BFO at compressive epitaxial strains and of the 20-atoms simulation cell used in most of our calculations; Bi, Fe, and O atoms are represented with purple, brown, and red spheres, respectively. The unit cells of the R- and T-phases are indicated with black solid lines. (b) Zero-temperature energy (←) and *c*/*a* ratio (→) results obtained in pure BFO as a function of epitaxial strain. "A-G" and "A-C" stand for antiferromagnetic spin order of G- and C-type, respectively. (c) Young's modulus (←) and antiphase oxygen octahedral distortions (→) calculated in pure and doped stoichiometric BFO thin films at $\eta = -4.5\%$.

The numerical uncertainty in our calculations is of the order of 1 GPa. We find a consistent mechanical softening of the system as the ionic radius of the dopant species is decreased. In particular, we find zero-temperature Young's moduli of 108, 101, and 100 GPa in pure, La-doped, and Ca-doped thin films, respectively. A Poisson ratio of 0.26 ± 0.01 is calculated in all the cases, which is in good agreement with the experimental data. Interestingly, a detailed structural analysis reveals the appearance of non-negligible antiphase oxygen octahedral rotations within the substrate plane (AFD_{xy}^{-}, that is, $a^{-}a^{-}a^{0}$ in Glazer's notation) in the doped thin films (see Figure 5c). The size of these AFD_{xy}^{-} distortions appears to be inversely proportional to ionic radius of the dopant species. We can conclude, therefore, that the mechanical softening found in our DFT calculations is likely due to the development of antiphase oxygen octahedral rotations, which are largest in the Ca-doped system. This conclusion appears to be consistent with our measurements in pure BFO thin films: the Young's modulus of the T-phase, in which AFD_{xy}^{-} distortions are practically missing (*i.e.*, of the order of 0.5°), is larger than that of the R-phase, in which AFD_{xy}^{-} distortions are fully developed (*i.e.*, of the order of 8−10°). Nevertheless, our zero-temperature DFT results obtained in stoichiometric systems cannot explain the origins of the large mechanical hardening observed in Ca-doped thin films. It is worth noticing that aliovalent doping in BFO thin films poses some challenges to DFT modeling. The usual oxidation state of Ca ions is +2, whereas that of Bi ions is +3, hence implying that the presence of crystalline and stoichiometric defects in the samples (*e.g.*, vacancies and dislocations) is very likely.[9]

In an attempt to understand the causes behind the large mechanical hardening observed in Ca-doped thin films, we analyzed the effects of oxygen vacancies on the resulting elastic properties (for this, we doubled the size of the simulation cell along the *c* direction and removed one oxygen atom from the enlarged simulation cell). Interestingly, our DFT results show that a decrease in oxygen content can actually increase the value of Young's modulus by ∼25% as compared to that calculated in the perfect stoichiometric case (*i.e.*, Y = 125 GPa). The reason for such a large increase of Y is a crystal volume reduction of ∼11% as compared to the stoichiometric case. This predicted volume shrinkage leads to a sizable increase in the value of the C_{12}, C_{13}, C_{23} elastic constants in the nonstoichiometric system (of up to 160% in the latter case), that in turn leads to an increase of the corresponding bulk and Young's moduli (45 and 25%, respectively). We note that the value of the shear modulus increases less abruptly than in the previous two cases (*i.e.*, 14%). In light of these simulation results, we may conclude that the likely cause behind the mechanical hardening observed in Ca-doped thin films is the presence of crystalline defects, for instance, oxygen vacancies.[9,30]

CONCLUSIONS

In summary, we have experimentally shown that there is a clear correlation between the local strain environment and isovalent and aliovalent doping in mixed phase BFO. We find a general trend of stiffness across morphotropic phase boundaries in all systems such that the T-phase is stiffer than the R-phase near the boundaries, and the T-phase near the boundary is relatively stiffer than the T-phase without R-phase in close vicinity. Moreover, we clearly demonstrate that the overall stiffness of pure T-phase in undoped, Ca-doped, and La-doped BFO thin films is different by statistical analysis of Young's moduli extracted from *F*−*D* measurements. Statistical measurements of transition threshold strengths of these materials also show distinct onset stress ranges for the phase transformation from T- to R-phase, revealing their different local strain environment and therefore mechanical softening and hardening effect due to isovalent and aliovalent doping, respectively. Zero-temperature first-principles calculations performed in stoichiometric systems reveal a correlation between mechanical softening and the appearance of antiphase oxygen octahedral rotations within the substrate (epitaxial) plane. The size of these antiferrodistortive distortions is shown to depend inversely on the ionic radius of the dopant species, which explains the mechanical softening observed in La-doped BFO thin films. In light of our simulation

DOI: 10.1021/acsnano.6b07869
ACS Nano 2017, 11, 2805−2813

results, the mechanical hardening observed in Ca-doped thin films can be understood in terms of the appearance of crystalline defects such as oxygen vacancies. Of all of the investigated materials, La-doped BFO exhibits extreme softening behavior and low strain states, leading to its characteristic feature of mixed phase regions with micron-long stripes. Our results thus give an insight of the tuning nanomechanical properties in BFO to enhance correlated functional properties and point to promising avenues for multifunctional applications.[43,46,50]

METHODS

Experimental Methods. All thin films were grown by pulsed laser deposition (PLD) with a KrF excimer laser (λ = 248 nm). Before the growth of the BFO layer, a conducting buffer layer of $Pr_{0.5}Ca_{0.5}MnO_3$ (pure and La-doped samples) and $La_{0.5}Sr_{0.5}CoO_3$ (Ca-doped sample) was deposited on a (001) $LaAlO_3$ substrate. Pure $BiFeO_3$ thin films were grown at 650 °C in 100 mTorr of oxygen pressure. The energy density was approximately 1 J/cm^2, and the frequency was 10 Hz. At the end of deposition, the sample was cooled down to room temperature at the rate of 10 °C/min in 500 Torr of oxygen. 2% Ca-doped $BiFeO_3$ thin films were grown at 700 °C in 100 mTorr of oxygen pressure. The energy density was approximately 1 J/cm^2, and the frequency was 2 Hz. Typical deposition rates were approximately 2 nm min^{-1}. The film was cooled down at the rate of 10 °C/min in 1 bar of oxygen. 5% La-doped $BiFeO_3$ thin films were grown at 650 °C in 100 mTorr of oxygen pressure. The energy density was approximately 0.7 J/cm^2, and the frequency was 10 Hz. A BLFO ceramic target ($Bi_{1.05}La_{0.05}FeO_3$) with a 10% excess Bi was used to prevent a loss of bismuth during deposition. The sample was cooled to room temperature at a rate of 10 °C/min in 500 Torr of oxygen.

The crystal structures and orientations of the thin films were analyzed using a conventional four-circle diffractometer (PANalytical X'Pert MRD) at UNSW Australia. For confirmation of crystal phases without strain effects and impurities, detailed investigations by θ-2θ scans in (002) direction and reciprocal space maps (RSMs) in (−103) orientation were carried out on the BFO samples. For the investigation of mechanical properties, we used a conventional AFM system (AIST-NT SmartSPM 1000), where we utilized AFM-tips (DCP20, NT-MDT) to apply force against the surface of BFO samples.

Computation Methods. We calculated the energy, structural properties, and elastic constants of BFO thin films (pure, La-doped, and Ca-doped) with first-principles DFT methods. We used the generalized gradient approximation to DFT due to Perdew, Burke, and Ernzerhof (GGA-PBE),[51] as it is implemented in the VASP package.[52,53] A "Hubbard-U" scheme with U = 4.0 eV was employed for a better treatment of Fe's 3d electrons.[48] We used the "projector augmented wave" method to represent the ionic cores,[54] considering the following electrons as valence states: Bi's 5d, 6s, and 6p; La's 4d, 5p, and 6s; Fe's 3s, 3p, and 3d; Ca's 3s, 3p, and 4s; and O's 2s and 2p. Wave functions were represented in a plane-wave basis truncated at 1100 eV. We used a 20-atoms $\sqrt{2} \times \sqrt{2} \times 2$ simulation cell that allows reproducing the usual ferroelectric and antiferrodistortive distortions observed in oxide perovskites[47] (see Figure 5a). Isovalent- and aliovalent-doped systems were generated by substituting one Bi atom in the simulation cell with one La or Ca atom, respectively. For integrations in the Brillouin zone (BZ), we employed a gamma-centered k-point grid of $6 \times 6 \times 6$. Spin-polarized geometry relaxations were performed using a conjugate-gradient algorithm that varied the volume and shape of the unit cell and fulfilled the lattice vector constraints applying to thin films; the imposed tolerance on the atomic force was 0.01 eV·Å^{-1}. By using these parameters, we obtained the total energy that was converged to within 0.5 meV per formula unit. The elastic constants were determined by performing finite distortions of the simulation cell and considering ionic contributions through the inversion of the Hessian matrix. Subsequently, we estimated the corresponding bulk and shear modulus, B and G, by using the Voigt−Reuss−Hill relations, which are appropriate for polycrystalline systems.[55] Finally, we obtained the value of the Young's modulus, Y, and Poisson ratio, ν, *via* the formulas $Y = 9BG/(3B + G)$ and $\nu = (3B - 2G)/[2(3B + G)]$.

AUTHOR INFORMATION

Corresponding Author

*E-mail: jan.seidel@unsw.edu.au.

ORCID

Jan Seidel: 0000-0003-2814-3241

Notes

The authors declare no competing financial interest.

ACKNOWLEDGMENTS

We acknowledge support by the Australian Research Council under grant nos. FT110100523, FT140100135, DP140100463, and DP140102849. This work was also supported by the National Research Foundation of Korea funded by the Ministry of Education, Science, and Technology (contract nos. NRF-2013S1A2A2035418 and 2016R1A5A1008184). Computational resources and technical assistance were provided by the Australian Government through Magnus under the National Computational Merit Allocation Scheme. This work was also partially supported by the Japan Science and Technology Agency, CREST, a Grant-in-Aid for Scientific Research (grant no. 24760009), and a grant for the Joint Project of Chemical Synthesis Core Research Institutions from the Ministry of Education, Culture, Sports, Science, and Technology of Japan.

REFERENCES

(1) Groth, P. Ueber Beziehungen Zwischen Krystallform Und Chemische Constitution Bei Einigen Organischen Verbindungen. *Ann. Phys.* **1870**, *217*, 31−43.

(2) Goldschmidt, V. M. Crystal Structure and Chemical Constitution. *Trans. Faraday Soc.* **1929**, *25*, 253−283.

(3) Noheda, B. Structure and High-Piezoelectricity in Lead Oxide Solid Solutions. *Curr. Opin. Solid State Mater. Sci.* **2002**, *6*, 27−34.

(4) Rödel, J.; Jo, W.; Seifert, K. T. P.; Anton, E.-M.; Granzow, T.; Damjanovic, D. Perspective on the Development of Lead-free Piezoceramics. *J. Am. Ceram. Soc.* **2009**, *92*, 1153−1177.

(5) Noheda, B.; Cox, D. E. Bridging Phases at the Morphotropic Boundaries of Lead Oxide Solid Solutions. *Phase Transitions* **2006**, *79*, 5−20.

(6) Ko, K.-T.; Jung, M. H.; He, Q.; Lee, J. H.; Woo, C. S.; Chu, K.; Seidel, J.; Jeon, B.-G.; Oh, Y. S.; Kim, K. H.; Liang, W.-I.; Chen, H.-J.; Chu, Y.-H.; Jeong, Y. H.; Ramesh, R.; Park, J.-H.; Yang, C.-H. Concurrent Transition of Ferroelectric and Magnetic Ordering near Room Temperature. *Nat. Commun.* **2011**, *2*, 567.

(7) Seidel, J.; Fu, D.; Yang, S.-Y.; Alarcón-Lladó, E.; Wu, J.; Ramesh, R.; Ager, J. W. III. Efficient Photovoltaic Current Generation at Ferroelectric Domain Walls. *Phys. Rev. Lett.* **2011**, *107*, 126805.

(8) Seidel, J. Domain Walls as Nanoscale Functional Elements. *J. Phys. Chem. Lett.* **2012**, *3*, 2905−2909.

(9) Yang, C. H.; Seidel, J.; Kim, S. Y.; Rossen, P. B.; Yu, P.; Gajek, M.; Chu, Y. H.; Martin, L. W.; Holcomb, M. B.; He, Q.; Maksymovych, P.; Balke, N.; Kalinin, S. V.; Baddorf, A. P.; Basu, S. R.; Scullin, M. L.; Ramesh, R. Electric Modulation of Conduction in Multiferroic Ca-Doped $BiFeO_3$ Films. *Nat. Mater.* **2009**, *8*, 485−493.

(10) Zeches, R. J.; Rossell, M. D.; Zhang, J. X.; Hatt, A. J.; He, Q.; Yang, C.-H.; Kumar, A.; Wang, C. H.; Melville, A.; Adamo, C.; Sheng, G.; Chu, Y.-H.; Ihlefeld, J. F.; Erni, R.; Ederer, C.; Gopalan, V.; Chen, L. Q.; Schlom, D. G.; Spaldin, N. A.; Martin, L. W.; Ramesh, R. A Strain-Driven Morphotropic Phase Boundary in $BiFeO_3$. *Science* **2009**, *326*, 977−980.

(11) Béa, H.; Dupé, B.; Fusil, S.; Mattana, R.; Jacquet, E.; Warot-Fonrose, B.; Wilhelm, F.; Rogalev, A.; Petit, S.; Cros, V.; Anane, A.; Petroff, F.; Bouzehouane, K.; Geneste, G.; Dkhil, B.; Lisenkov, S.;

DOI: 10.1021/acsnano.6b07869
ACS Nano 2017, 11, 2805−2813

Ponomareva, I.; Bellaiche, L.; Bibes, M.; Barthélémy, A. Evidence for Room-Temperature Multiferroicity in a Compound with a Giant Axial Ratio. *Phys. Rev. Lett.* **2009**, *102*, 217603.
(12) MacDougall, G. J.; Christen, H. M.; Siemons, W.; Biegalski, M. D.; Zarestky, J. L.; Liang, S.; Dagotto, E.; Nagler, S. E. Antiferromagnetic transitions in tetragonal-like $BiFeO_3$. *Phys. Rev. B: Condens. Matter Mater. Phys.* **2012**, *85*, 100406.
(13) Farokhipoor, S.; Noheda, B. Conduction through 71° Domain Walls in $BiFeO_3$ Thin Films. *Phys. Rev. Lett.* **2011**, *107*, 127601.
(14) Chiu, Y.-P.; Chen, Y.-T.; Huang, B.-C.; Shih, M.-C.; Yang, J.-C.; He, Q.; Liang, C.-W.; Seidel, J.; Chen, Y.-C.; Ramesh, R.; Chu, Y.-H. Atomic-Scale Evolution of Local Electronic Structure across Multiferroic Domain Walls. *Adv. Mater.* **2011**, *23*, 1530−1534.
(15) Lubk, A.; Gemming, S.; Spaldin, N. A. First-Principles Study of Ferroelectric Domain Walls in Multiferroic Bismuth Ferrite. *Phys. Rev. B: Condens. Matter Mater. Phys.* **2009**, *80*, 104110.
(16) Lubk, A.; Rossell, M. D.; Seidel, J.; Chu, Y. H.; Ramesh, R.; Hÿtch, M. J.; Snoeck, E. Electromechanical Coupling among Edge Dislocations, Domain Walls, and Nanodomains in $BiFeO_3$ Revealed by Unit-Cell-Wise Strain and Polarization Maps. *Nano Lett.* **2013**, *13*, 1410−1415.
(17) Lubk, A.; Rossell, M. D.; Seidel, J.; He, Q.; Yang, S. Y.; Chu, Y. H.; Ramesh, R.; Hÿtch, M. J.; Snoeck, E. Evidence of Sharp and Diffuse Domain Walls in $BiFeO_3$ by Means of Unit-Cell-Wise Strain and Polarization Maps Obtained with High Resolution Scanning Transmission Electron Microscopy. *Phys. Rev. Lett.* **2012**, *109*, 047601.
(18) Chu, K.; Jang, B.-K.; Sung, J. H.; Shin, Y. A.; Lee, E.-S.; Song, K.; Lee, J. H.; Woo, C.-S.; Kim, S. J.; Choi, S.-Y.; Koo, T. Y.; Kim, Y.-H.; Oh, S.-H.; Jo, M.-H.; Yang, C.-H. Enhancement of the Anisotropic Photocurrent in Ferroelectric Oxides by Strain Gradients. *Nat. Nanotechnol.* **2015**, *10*, 972−979.
(19) Kan, D.; Pálová, L.; Anbusathaiah, V.; Cheng, C. J.; Fujino, S.; Nagarajan, V.; Rabe, K. M.; Takeuchi, I. Universal Behavior and Electric-Field-Induced Structural Transition in Rare-Earth-Substituted $BiFeO_3$. *Adv. Funct. Mater.* **2010**, *20*, 1108−1115.
(20) Zhang, J. X.; Xiang, B.; He, Q.; Seidel, J.; Zeches, R. J.; Yu, P.; Yang, S. Y.; Wang, C. H.; Chu, Y. H.; Martin, L. W.; Minor, A. M.; Ramesh, R. Large Field-Induced Strains in a Lead-Free Piezoelectric Material. *Nat. Nanotechnol.* **2011**, *6*, 98−102.
(21) Christen, H. M.; Nam, J. H.; Kim, H. S.; Hatt, A. J.; Spaldin, N. A. Stress-induced R-R-M_A-M_C-T symmetry changes in $BiFeO_3$ films. *Phys. Rev. B: Condens. Matter Mater. Phys.* **2011**, *83*, 144107.
(22) Yang, C.-H.; Kan, D.; Takeuchi, I.; Nagarajan, V.; Seidel, J. Doping $BiFeO_3$: approaches and enhanced functionality. *Phys. Chem. Chem. Phys.* **2012**, *14*, 15953−15962.
(23) Zhang, J. X.; He, Q.; Trassin, M.; Luo, W.; Yi, D.; Rossell, M. D.; Yu, P.; You, L.; Wang, C. H.; Kuo, C. Y.; Heron, J. T.; Hu, Z.; Zeches, R. J.; Lin, H. J.; Tanaka, A.; Chen, C. T.; Tjeng, L. H.; Chu, Y. H.; Ramesh, R. Microscopic Origin of the Giant Ferroelectric Polarization in Tetragonal-like $BiFeO_3$. *Phys. Rev. Lett.* **2011**, *107*, 147602.
(24) Chen, Y.-C.; He, Q.; Chu, F.-N.; Huang, Y.-C.; Chen, J.-W.; Liang, W.-I.; Vasudevan, R. K.; Nagarajan, V.; Arenholz, E.; Kalinin, S. V.; Chu, Y.-H. Electrical Control of Multiferroic Orderings in Mixed-Phase $BiFeO_3$ Films. *Adv. Mater.* **2012**, *24*, 3070−3075.
(25) Vasudevan, R. K.; Chen, Y.-C.; Tai, H.-H.; Balke, N.; Wu, P.; Bhattacharya, S.; Chen, L. Q.; Chu, Y.-H.; Lin, I. N.; Kalinin, S. V.; Nagarajan, V. Exploring Topological Defects in Epitaxial $BiFeO_3$ Thin Films. *ACS Nano* **2011**, *5*, 879−887.
(26) Zhou, J.; Trassin, M.; He, Q.; Tamura, N.; Kunz, M.; Cheng, C.; Zhang, J.; Liang, W.-I.; Seidel, J.; Hsin, C.-L.; Wu, J. Directed Assembly of Nano-Scale Phase Variants in Highly Strained $BiFeO_3$ Thin Films. *J. Appl. Phys.* **2012**, *112*, 064102.
(27) Zhang, J.; Ke, X.; Gou, G.; Seidel, J.; Xiang, B.; Yu, P.; Liang, W.-I.; Minor, A. M.; Chu, Y.-h.; Van Tendeloo, G.; Ren, X.; Ramesh, R. A Nanoscale Shape Memory Oxide. *Nat. Commun.* **2013**, *4*, 2768.
(28) Guide, M.; Dang, X.-D.; Nguyen, T.-Q. Nanoscale Characterization of Tetrabenzoporphyrin and Fullerene-Based Solar Cells by Photoconductive Atomic Force Microscopy. *Adv. Mater.* **2011**, *23*, 2313−2319.
(29) Lee, J. H.; Chu, K.; Ünal, A. A.; Valencia, S.; Kronast, F.; Kowarik, S.; Seidel, J.; Yang, C.-H. Phase separation and electrical switching between two isosymmetric multiferroic phases in tensile strained $BiFeO_3$ thin films. *Phys. Rev. B: Condens. Matter Mater. Phys.* **2014**, *89*, 140101.
(30) Seidel, J.; Trassin, M.; Zhang, Y.; Maksymovych, P.; Uhlig, T.; Milde, P.; Köhler, D.; Baddorf, A. P.; Kalinin, S. V.; Eng, L. M.; Pan, X.; Ramesh, R. Electronic Properties of Isosymmetric Phase Boundaries in Highly Strained Ca-Doped $BiFeO_3$. *Adv. Mater.* **2014**, *26*, 4376−4380.
(31) Heo, Y.; Jang, B.-K.; Kim, S. J.; Yang, C.-H.; Seidel, J. Nanoscale Mechanical Softening of Morphotropic $BiFeO_3$. *Adv. Mater.* **2014**, *26*, 7568−7572.
(32) Sharma, P.; Heo, Y.; Jang, B.-K.; Liu, Y.; Nagarajan, V.; Li, J.; Yang, C.-H.; Seidel, J. Morphotropic Phase Elasticity of Strained BiFeO3. *Adv. Mater. Interfaces* **2016**, *3*, 1600033.
(33) Ikeda-Ohno, A.; Lim, J. S.; Ohkochi, T.; Yang, C.-H.; Seidel, J. Investigation of Continuous Changes in the Electric-Field-Induced Electronic State in $Bi_{1-X}Ca_xFeO_{3-\delta}$. *Phys. Chem. Chem. Phys.* **2014**, *16*, 17412−17416.
(34) Seidel, J.; Luo, W.; Suresha, S. J.; Nguyen, P. K.; Lee, A. S.; Kim, S. Y.; Yang, C. H.; Pennycook, S. J.; Pantelides, S. T.; Scott, J. F.; Ramesh, R. Prominent electrochromism through vacancy-order melting in a complex oxide. *Nat. Commun.* **2012**, *3*, 799.
(35) You, L.; Caesario, P.; Fang, L.; Ren, P.; Wang, L.; Zhou, Y.; Gruverman, A.; Wang, J. Effect of Lanthanum Doping on Tetragonal-Like $BiFeO_3$ with Mixed-Phase Domain Structures. *Phys. Rev. B: Condens. Matter Mater. Phys.* **2014**, *90*, 134110.
(36) Kim, K.-E.; Jang, B.-K.; Heo, Y.; Hong Lee, J.; Jeong, M.; Lee, J. Y.; Seidel, J.; Yang, C.-H. Electric Control of Straight Stripe Conductive Mixed-Phase Nanostructures in La-Doped $BiFeO_3$. *NPG Asia Mater.* **2014**, *6*, e81.
(37) Redfern, S. A. T.; Can, W.; Hong, J. W.; Catalan, G.; Scott, J. F. Elastic and Electrical Anomalies at Low-Temperature Phase Transitions in $BiFeO_3$. *J. Phys.: Condens. Matter* **2008**, *20*, 452205.
(38) Gavriliuk, A. G.; Struzhkin, V. V.; Lyubutin, I. S.; Ovchinnikov, S. G.; Hu, M. Y.; Chow, P. Another Mechanism for the Insulator-Metal Transition Observed in Mott Insulators. *Phys. Rev. B: Condens. Matter Mater. Phys.* **2008**, *77*, 155112.
(39) Shang, S. L.; Sheng, G.; Wang, Y.; Chen, L. Q.; Liu, Z. K. Elastic Properties of Cubic and Rhombohedral $BiFeO_3$ from First-Principles Calculations. *Phys. Rev. B: Condens. Matter Mater. Phys.* **2009**, *80*, 052102.
(40) Vasudevan, R. K.; Okatan, M. B.; Liu, Y. Y.; Jesse, S.; Yang, J. C.; Liang, W. I.; Chu, Y. H.; Li, J. Y.; Kalinin, S. V.; Nagarajan, V. Unraveling the Origins of Electromechanical Response in Mixed-Phase Bismuth Ferrite. *Phys. Rev. B: Condens. Matter Mater. Phys.* **2013**, *88*, 020402.
(41) You, L.; Chen, Z.; Zou, X.; Ding, H.; Chen, W.; Chen, L.; Yuan, G.; Wang, J. Characterization and Manipulation of Mixed Phase Nanodomains in Highly Strained $BiFeO_3$ Thin Films. *ACS Nano* **2012**, *6*, 5388−5394.
(42) Cheng, C.-E.; Liu, H.-J.; Dinelli, F.; Chen, Y.-C.; Chang, C.-S.; Chien, F. S.-S.; Chu, Y.-H. Revealing the Flexoelectricity in the Mixed-Phase Regions of Epitaxial $BiFeO_3$ Thin Films. *Sci. Rep.* **2015**, *5*, 8091.
(43) Sharma, P.; Heo, Y.; Jang, B. K.; Liu, Y. Y.; Li, J. Y.; Yang, C. H.; Seidel, J. Structural and Electronic Transformation Pathways in Morphotropic $BiFeO_3$. *Sci. Rep.* **2016**, *6*, 32347.
(44) Kaya, S.; Yilmaz, E.; Aktag, A.; Seidel, J. Characterization of Interface Defects in $BiFeO_3$ Metal−Oxide−Semiconductor Capacitors Deposited by Radio Frequency Magnetron Sputtering. *J. Mater. Sci.: Mater. Electron.* **2015**, *26*, 5987−5993.
(45) Kaya, S.; Lok, R.; Aktag, A.; Seidel, J.; Yilmaz, E. Frequency Dependent Electrical Characteristics of $BiFeO_3$ MOS Capacitors. *J. Alloys Compd.* **2014**, *583*, 476−480.

DOI: 10.1021/acsnano.6b07869
ACS Nano 2017, 11, 2805−2813

(46) Martin, L. W.; Chu, Y.-H.; Ramesh, R., Emerging Multiferroic Memories. In *Emerging Non-Volatile Memories*, Hong, S., Auciello, O., Wouters, D., Eds.; Springer US: Boston, MA, 2014; pp 103−166.
(47) Cazorla, C.; Stengel, M. Electrostatic Engineering of Strained Ferroelectric Perovskites from First Principles. *Phys. Rev. B: Condens. Matter Mater. Phys.* **2015**, *92*, 214108.
(48) Cazorla, C.; Íñiguez, J. Insights into the Phase Diagram of Bismuth Ferrite from Quasiharmonic Free-Energy Calculations. *Phys. Rev. B: Condens. Matter Mater. Phys.* **2013**, *88*, 214430.
(49) Escorihuela-Sayalero, C.; Diéguez, O.; Íñiguez, J. Strain Engineering Magnetic Frustration in Perovskite Oxide Thin Films. *Phys. Rev. Lett.* **2012**, *109*, 247202.
(50) Scullin, M. L.; Yu, C.; Huijben, M.; Mukerjee, S.; Seidel, J.; Zhan, Q.; Moore, J.; Majumdar, A.; Ramesh, R. Anomalously Large Measured Thermoelectric Power Factor in $Sr_{1-X}La_xTiO_3$ Thin Films Due to $SrTiO_3$ Substrate Reduction. *Appl. Phys. Lett.* **2008**, *92*, 202113.
(51) Perdew, J. P.; Burke, K.; Ernzerhof, M. Generalized Gradient Approximation Made Simple. *Phys. Rev. Lett.* **1996**, *77*, 3865−3868.
(52) Kresse, G.; Furthmüller, J. Efficient Iterative Schemes for Ab Intio Total-Energy Calculations Using a Plane-Wave Basis Set. *Phys. Rev. B: Condens. Matter Mater. Phys.* **1996**, *54*, 11169−11186.
(53) Kresse, G.; Joubert, D. From Ultrasoft Pseudopotentials to the Projector Augmented-Wave Method. *Phys. Rev. B: Condens. Matter Mater. Phys.* **1999**, *59*, 1758−1775.
(54) Blöchl, P. E. Projector Augmented-Wave Method. *Phys. Rev. B: Condens. Matter Mater. Phys.* **1994**, *50*, 17953−17979.
(55) Ivanovskii, A. L. Mechanical and Electronic Properties of Diborides of Transition 3d-5d Metals from First Principles: Toward Search of Novel Ultra-Incompressible and Superhard Materials. *Prog. Mater. Sci.* **2012**, *57*, 184−228.

DOI: 10.1021/acsnano.6b07869
ACS Nano 2017, 11, 2805−2813